Journal of
Materials Chemistry A

PAPER

View Article Online
View Journal | View Issue

Cite this: *J. Mater. Chem. A*, 2024, **12**, 21864

Interface engineering and oxygen vacancies derived from plasma-treated Cu_2O synergistically enhancing electrocatalytic CO_2-to-C_{2+} conversion†

Lei Wang,‡[ab] Xue Yao,‡[c] Subhajit Jana,‡[a] Yongzan Zhou,‡[a] Chunlan Qin,[d]
Hongwei Shou,[d] Youchao Teng,[a] Ning Chen,[e] Lidong Zhang,[c]
Chandra Veer Singh,*[cf] Zhongchao Tan*[ag] and Yimin A. Wu*[abh]

Received 20th May 2024
Accepted 15th July 2024

DOI: 10.1039/d4ta03492a

rsc.li/materials-a

Electrocatalytic CO_2 reduction (ECR) into value-added chemicals and fuels helps tackle the challenges of the energy crisis and global warming. However, this strategy relies heavily on the rational design of catalysts with high selectivity and activity towards C_{2+} products. Herein, we introduce a dual-engineering strategy using plasma-treated Cu_2O to synergistically enhance the material's catalytic performance for CO_2-to-C_{2+} conversion. We demonstrate that well-controlled plasma reduction treatment in an Ar/H_2 atmosphere can yield stable Cu_2O–Cu catalysts (Cu_2O–Ar/H_2) with Cu^0/Cu^+ interfaces, abundant grain boundaries, and a high density of oxygen vacancies. Cu_2O–Ar/H_2 delivers an impressive 81.2% faradaic efficiency for C_{2+} products at an industrial current density of 100 mA cm^{-2}. Performance comparisons show that plasma pre-reduction treatment samples outperform the *in situ* reduced Cu_2O sample during ECR. Theoretical calculations reveal that the well-defined Cu^0/Cu^+ interfaces optimize intermediate adsorption and the oxygen vacancies provide multiple active sites for C–C coupling. This work establishes a correlation between plasma treatment-generated active sites and high C_{2+} product selectivity. Our work also demonstrates that this facile, scalable, standardized and controllable material preparation method can effectively promote the large-scale application of high-activity ECR catalysts.

1 Introduction

Electrocatalytic CO_2 reduction (ECR) into high-value chemicals and feedstocks using renewable electricity offers an elegant solution for closing the carbon cycle, addressing global environmental issues, and meeting growing energy demands.[1,2] However, the potential of this technology heavily relies on the development of highly active and selective electrocatalysts.[3,4] Although other metals such as Ag and Sn have achieved highly selective C_1 products, such as CO and formate,[5,6] achieving high selectivity for C_{2+} products on Cu-based catalysts remains highly challenging due to their sluggish multiple proton-coupled electron transfer (PCET) processes in C–C coupling and the competitive hydrogen evolution reaction (HER).[7] Therefore, there is an urgent need to develop highly efficient and active catalysts with scalable synthesis methods that can enhance selectivity towards C_{2+} products.

To enhance ECR to C_{2+} conversion selectivity, substantial efforts have focused on the rational design of copper-based catalysts, including morphology,[8] oxide-derived copper (OD-Cu),[9] interfacial structures,[10,11] and alloying[12,13] strategies. In particular, OD-Cu has been reported with excellent C_{2+} selectivity,[4] garnering widespread research interest. However, for OD-Cu, the active Cu^+ species inevitably undergoes electrochemical reduction to bulk metallic Cu at high current densities,[14] leading to poor selectivity for C_{2+} products. This poses a significant challenge for the effective utilization of OD-Cu. Thus, unconventional and feasible strategies for stabilizing the active Cu^+ species at reduction potentials during actual CO_2

---

[a] Department of Mechanical and Mechatronics Engineering, University of Waterloo, Waterloo, Ontario N2L 3G1, Canada. E-mail: yimin.wu@uwaterloo.ca

[b] Waterloo Institute for Nanotechnology, University of Waterloo, Waterloo, Ontario N2L 3G1, Canada

[c] Department of Materials Science and Engineering, University of Toronto, Toronto, Ontario M5S 3E4, Canada. E-mail: chandraveer.singh@utoronto.ca

[d] National Synchrotron Radiation Laboratory, University of Science and Technology of China, Hefei 230029, P. R. China

[e] Canadian Light Source, Saskatoon, SK S7N 2V3, Canada

[f] Department of Mechanical and Industrial Engineering, University of Toronto, Toronto, Ontario M5S 3G8, Canada

[g] Eastern Institute of Technology, No. 568 Tongxin Road, Zhenhai District, Ningbo, Zhejiang, 315200, China. E-mail: ztan@eitech.edu.cn

[h] Department of Chemistry, University of Waterloo, Waterloo, Ontario N2L 3G1, Canada

† Electronic supplementary information (ESI) available. See DOI: https://doi.org/10.1039/d4ta03492a

‡ Equal contributions.

reduction processes is necessary. Research results indicate that abundant nanograin boundaries can enhance the stability of catalyst morphology and Cu^0/Cu^+ interfaces at high polarization and high current density, preventing catalyst reconstruction and improving the catalytic stability.[15] Moreover, nanograin boundaries and the Cu^0/Cu^+ interface can increase *CO adsorption strength, promoting CO–CO coupling toward C_{2+} products.[16,17] Therefore, constructing intricate structures assembled with abundant nanograin boundaries and Cu^0/Cu^+ interfaces in Cu-based catalysts is promising for achieving efficient ECR to C_{2+} products.

In addition, oxygen vacancies, as a well-known defect, are widely employed to tailor the properties of catalysts.[18–20] For example, due to their weakly bound electrons, oxygen vacancies serve as excellent Lewis base sites to enhance the binding affinities of key intermediates (such as *CO and *COH), thereby promoting the production of C_2.[21] Moreover, a higher concentration of oxygen vacancies near the active sites is favorable for activating CO_2 molecules, lowering the reaction barrier for targeted products.[22] Therefore, integrating oxygen vacancies with grain boundaries and interface engineering is likely to modulate the surface electronic structure and concentration of active sites, accelerating reaction kinetics. However, effectively constructing oxygen vacancies and interface structures on the catalyst surface is highly challenging. A deeper understanding of the synergistic interaction between oxygen vacancies and interface structures will provide valuable guidance for the rational design of catalysts.

Plasma treatment, as a facile and scalable technique, has been introduced to selectively activate catalysts, due to its ability to rapidly alter the surface chemical state of catalysts at room temperature,[23] create defect structures,[24] or embed heteroatoms[25] to improve reactivity. For example, Cu surfaces treated with O_2 plasma exhibit higher ethylene selectivity than those treated with H_2 plasma. The activity enhancement may originate from the presence of Cu^+.[26] Cuenya's group reported that O_2 plasma treatment gives rise to specific defect sites and stable subsurface oxygen species inside Cu nanocubes, which are key to achieving high activity and ethylene selectivity.[27] Additionally, Kang's group indicated that oxygen-plasma-assisted nitrogen doping on CuO can achieve high C_{2+} product selectivity, with enhanced activity attributed to the oxygen vacancies and grain boundary defects generated by N_2 plasma radicals on CuO.[24] These studies suggest that plasma treatment, as an effective surface treatment method, can precisely control active sites under different atmospheres.[28,29] Nevertheless, whether plasma treatment can be used to synergistically construct oxygen vacancies and Cu^+/Cu^0 interface structures on the metal oxide catalyst surface has yet to be investigated.

In this study, we employ plasma treatment under different atmospheres as a dual-engineering strategy to couple oxygen vacancies and interface structures, aiming to enhance the activity of the ECR catalysts. Plasma treatment in an Ar/H_2 environment results in the reduction of grain-boundary-rich Cu_2O, creating active interfaces of Cu^0/Cu^+ interface structures and abundant oxygen vacancies. Compared to original Cu_2O and Cu_2O treated under an Ar/O_2 atmosphere (Cu_2O–Ar/O_2), the coordinated interaction between Cu^0/Cu^+ and oxygen vacancies from Cu_2O–Ar/H_2 contributes to enhanced catalytic activity for C_{2+} products. DFT calculations indicate that Cu_2O–Ar/H_2 is more favorable for *OHCCO intermediate adsorption, promoting the conversion of C_{2+} products. As a result, the Cu_2O–Ar/H_2 sample achieves a faradaic efficiency of 81.4% for C_{2+} products at a current density of 100 mA cm^{-2}. This study reveals the mechanism by which plasma treatment enhances catalyst activity, advancing the development of ECR to C_{2+} products.

2 Experimental section

2.1 Materials

A Cu_2O target was purchased from AJA International Inc, USA. Potassium hydroxide (KOH) and ultrapure water (18 MΩ cm) were obtained from the University of Waterloo Chemical Store. Carbon paper (Freudenberg H15C13) and a Fumasep FAB-PK-130 membrane were purchased from a fuel cell store, USA. Argon and CO_2 gas were provided by Linde Gas, Canada.

2.2 Synthesis of electrocatalysts

2.2.1 Synthesis of Cu_2O nanostructures. The carbon paper was cut into pieces of size 6 cm × 4 cm and then gently (low power) sonicated in acetone and IPA for 5 minutes each to remove any unbound materials or surface impurities. The substrates were then dried with an N_2 blower and heated at 80 ° C for 30 minutes to remove any solvent residue. After that, Cu_2O was sputter-deposited on the substrates. For sputtering, the base pressure of the deposition chamber was $\sim 2 \times 10^{-7}$ torr, and the Cu_2O target was pre-sputtered for 30 min at 200 W. After that, the clean substrates were soaked at 70 °C for 30 minutes inside the deposition chamber and then sputtered for 90 minutes at 200 W power (DC bias: 380 V), keeping the Ar and O_2 flow fixed at 12 sccm and 0.3 sccm, respectively with a 3 mTorr chamber pressure during deposition.

2.2.2 Plasma treatment. The substrates were again cut into small pieces of size 2 cm × 2 cm and then treated with two different plasmas under different atmospheres, keeping all other parameters the same. For plasma treatment, the chamber was flushed with Ar gas three times before each treatment, and the chamber pressure was maintained at 100 mTorr and with an RIE and ICP power of 100 W each. Two different plasmas were created as per the set parameters with different gas flows as follows: O_2 plasma: O_2 flow 45 sccm, Ar flow 5 sccm; and H_2 plasma: H_2 flow 15 sccm, Ar flow 35 sccm.

2.3 *Ex situ* material characterization

Scanning electron microscopy (SEM, Hitachi S4800, Japan) images were taken with a working accelerating voltage of 10 kV. Glancing-incidence X-ray diffraction (GIXRD) spectra were collected on a MRD diffractometer (PANalytical X'Pert Pro, Netherlands) with Cu Kα radiation (1.54 Å) at an incidence angle of 0.3°. X-ray photoelectron spectroscopy (XPS) measurements were conducted (Thermo-VG Scientific ESCALab 250, USA) using microprobes with a monochromatic Al Kα X-ray source (1486.6 eV). High resolution TEM images (Zeiss Libra 200 MC, German) were collected with an acceleration voltage of 200 kV. The XAS measurements were conducted at the 06ID-1 Hard X-ray MicroAnalysis (HXMA) beamline of the Canadian Light Source (CLS) operated at 2.9 GeV with a constant current of 220 mA. The measurements at the copper K-edge were performed in fluorescence mode using a Ge detector. Proton nuclear magnetic resonance (H-NMR) spectroscopy was run on a Bruker Avance III 500 MHz, USA. The reduced products were evaluated on a gas chromatograph (Shimadzu, GC-2014) with a Carbonxen® 1000 column and a CarbonPLOT column for a flame ionization detector (FID) and thermal conductivity detector (TCD), respectively.

2.4 Electrochemical measurements

For the ECR test, all electrochemical tests were performed using an electrochemical workstation (Gamry Reference 3000) with *iR* compensation at room temperature. The performance evaluation of electrochemical CO_2 reduction is conducted in flow cell setups. A prepared sample on carbon paper, Ni foam, and Ag/AgCl are used as the working electrode, counter electrode, and reference electrode, respectively. A gas-tight three-chamber flow cell is equipped with a Fumasep FAB-PK-130 anion exchange membrane (AEM), and 1 M KOH serves as the cathode and anode circulating electrolyte with a flow rate of 18 mL min^{-1}. The flow rate of CO_2 gas is set to 30 sccm. The ECR catalytic activities were evaluated using the potentiostatic technique for 1000 s. The gas products were analyzed using a Shimadzu GC-2014, while the liquid products were characterized using a Bruker 500 MHz Nuclear Magnetic Resonance (NMR) spectrometer with an internal reference prepared with D_2O and DMSO.

All potentials in this work were measured against the Ag/AgCl reference electrode and converted into reversible hydrogen potential (RHE) using the equation below:

$$E(vs.\ \mathrm{RHE}) = E(vs.\ \mathrm{Ag/AgCl}) + 0.059 \times \mathrm{pH} + 0.197$$

All the potentials are relative to the RHE unless stated otherwise.

2.5 DFT calculation details

All calculations were performed using the Vienna *ab initio* simulation package with the Perdew–Burke–Ernzerhof (PBE) generalized gradient approximation (GGA) exchange–correlation functional.[30] A plane wave cutoff energy of 450 eV was employed. Spin polarization and van der Waals corrections in the models were accounted for using the projector augmented wave (PAW)[31] method and DFT-D3,[32] respectively. The convergence criteria for the total energy and forces were set to 1×10^{-5} eV and 0.03 eV $Å^{-1}$, respectively. The *k*-point sampling was performed using a $3 \times 3 \times 1$ gamma scheme. A vacuum layer of 15 Å was introduced to eliminate interactions between the layers in the model. A three-layer Cu_2O (111) surface was constructed to model the Cu_2O sample, where the oxygen vacancy on the Cu_2O (111) surface is represented by removing a coordinated oxygen atom (Fig. S11a†). The Cu_2O (111)/Cu (111) structure was obtained by adding two layers of Cu (111) under the Cu_2O (111) surface, a four-layer slab model, to model the Cu_2O–Ar/H_2 sample (Fig. S11b†). The VASPsol implicit solvation model was used to study the solvation effect.[33] As shown in Table S3†, taking two key intermediates of the potential-determining steps, *CO and *CHO, as examples, there is little difference in the reaction energies considering the solvation effect or not, and consequently the solvation effect is not considered.

3 Results and discussion

3.1 Synthesis and *ex situ* characterization of electrocatalysts

The material preparation process, involving both magnetron sputtering and plasma treatment, is illustrated in Fig. 1a. Initially, Cu_2O catalysts are fabricated on a gas diffusion electrode (GDE) *via* magnetron sputtering using a Cu_2O target. Subsequently, plasma treatments on Cu_2O catalysts are conducted under reducing (Ar/H_2) and oxidizing (Ar/O_2) atmospheres, wherein highly reactive Ar/H_2 and Ar/O_2 active particles in the plasma state bombard the surface of Cu_2O, causing further reduction or oxidation. This would create different structural defects in the resulting Cu_2O–Ar/H_2 and Cu_2O–Ar/O_2. This facile and scalable material preparation method makes it feasible to produce large-scale gas diffusion electrode (GDE)-compatible high-activity ECR catalysts.

The composition and structural characteristics of the synthesized samples were investigated using grazing incidence X-ray diffraction (GIXRD). Diffraction peaks attributed to cuprite (Cu_2O JCPDF#05-0667) are observed in the Cu_2O and Cu_2O–Ar/O_2 samples (Fig. 1b), indicating that Ar/O_2 plasma treatment does not reduce the original Cu_2O. However, the mixed phase of Cu (JCPDF#04-0836) and Cu_2O in the Cu_2O–Ar/H_2 sample suggests that Ar/H_2 plasma treatment partially reduced Cu_2O to metallic copper (Fig. 1b), forming interface structures between Cu and Cu_2O. The scanning electron microscope (SEM) images reveal that Cu_2O nanoparticles are *in situ* grown on carbon paper using magnetron sputtering (Fig. S1a and b†). The Ar/H_2 (Fig. 1c, d, S1c and d†) and Ar/O_2 (Fig. S1e and f†) plasma treatments do not visibly affect the morphology of Cu_2O NPs. SEM-EDS elemental mapping images show a uniform distribution of Cu and O in the Cu_2O (Fig. S2a†) and Cu_2O–Ar/O_2 (Fig. S2b†) samples, while SEM-EDS images (Fig. 1e) confirm that Ar/H_2 plasma treatment does not completely reduce Cu_2O to Cu, as oxygen signals are still detected. Correspondingly, in terms of elemental composition, compared to pristine Cu_2O (Fig. S4†), the oxygen content in Cu_2O–Ar/H_2 (Fig. S3†) is significantly reduced, while the oxygen content in Cu_2O–Ar/O_2 (Fig. S5†) remains relatively unchanged. High-resolution transmission electron microscopy (HRTEM) images reveal the presence of abundant grain boundary structures in the as-synthesized samples (Fig. 1f and g). For the original Cu_2O, lattice spacings of 0.29 nm and 0.24 nm are attributed to the (110) and (111) planes of Cu_2O[34] (Fig. 1f and S6a and b†), respectively. However, after plasma

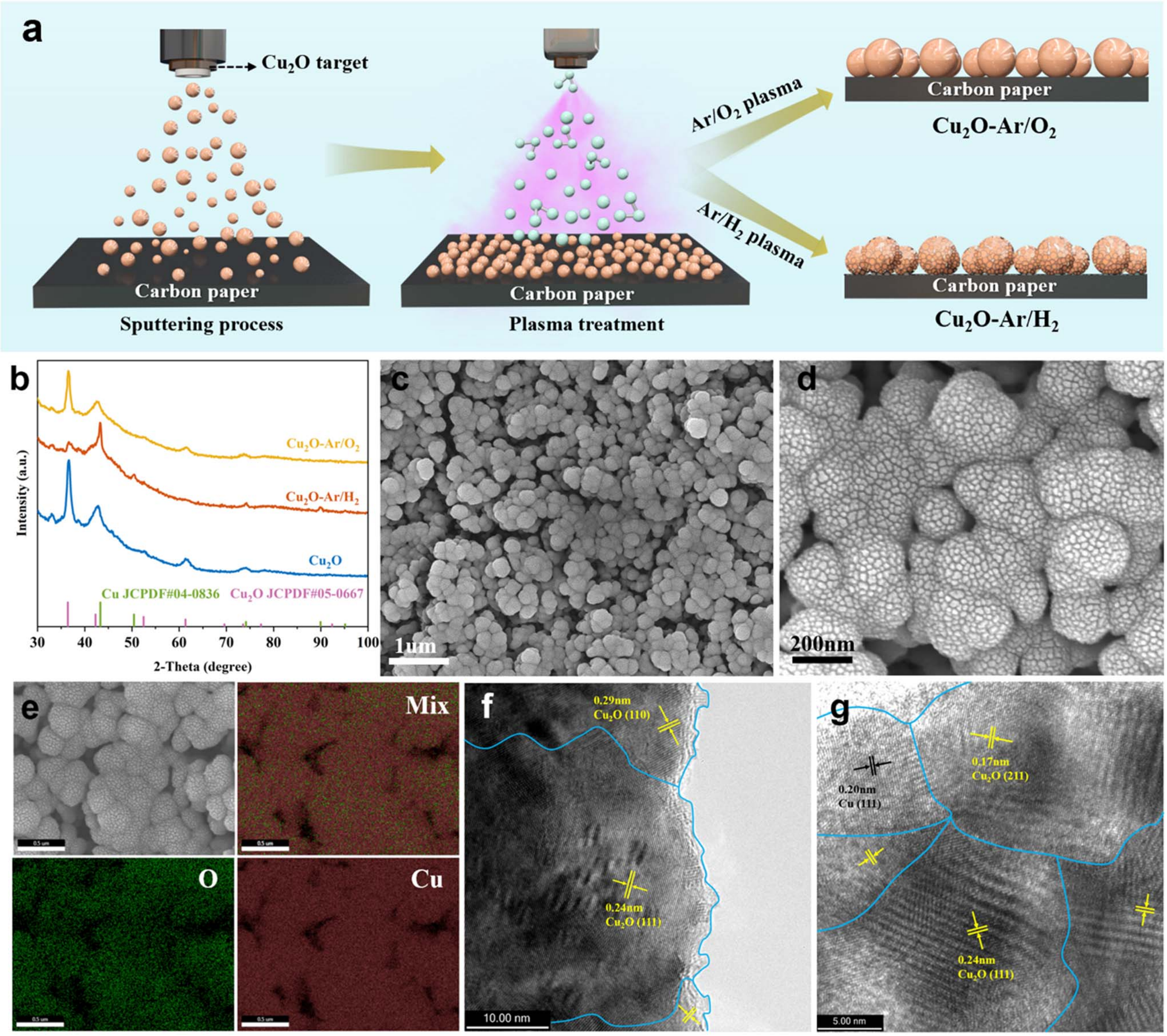

Fig. 1 Synthesis and structural characterization of electrocatalysts. (a) The schematic illustration of the as-synthesized catalysts. (b) GIXRD spectra of the as-prepared electrocatalysts; (c and d) SEM images of Cu_2O–Ar/H_2; (e) SEM-EDS elemental mapping images of Cu_2O–Ar/H_2; (f and g) HRTEM images of Cu_2O (f) and Cu_2O–Ar/H_2 (g).

reduction treatment on the Cu_2O–Ar/H_2 sample, the grain boundary structures observed at 0.17 nm for Cu_2O (211), 0.20 nm for Cu (111), and 0.24 nm for Cu_2O (111) indicate the existence of Cu^0/Cu^+ interface structures[35,36] (Fig. 1g and S7a†). This suggests that partial reduction of Cu atoms in Cu_2O nanoparticles has occurred under plasma reduction treatment, forming an interface between Cu^0 and Cu^+ within the Cu_2O lattice. Such interface structures may facilitate the formation of active sites and the generation of oxygen vacancies, thereby enhancing catalytic performance. In contrast, for the Cu_2O–Ar/O_2 sample, only the grain boundary structures of Cu_2O (111) and (110) are observed, with no presence of metallic Cu (Fig. S7b†). This indicates that the plasma oxidation process does not create the unique interface structure seen in the Cu_2O–Ar/H_2 sample.

X-ray photoelectron spectroscopy (XPS) was used to reveal changes in surface composition and chemical states of Cu_2O samples treated with plasma under different reaction atmospheres. For the Cu_2O and Cu_2O–Ar/H_2 samples, the Cu 2p XPS spectrum can be deconvoluted into two peaks at 932.4 and 933.9 eV, corresponding to Cu^+/Cu^0 and Cu^{2+} species[21,37] (Fig. S8†), respectively. However, compared to the samples treated with Ar/H_2 plasma reduction, those treated with Ar/O_2 plasma only exhibit features of Cu^{2+} species (Fig. S8†), indicating that the surface Cu_2O has been further oxidized. The Cu Auger LMM spectrum is employed to further confirm the valence state of the Cu species. For the original Cu_2O sample, the surface Cu is mainly in the monovalent and divalent Cu species.[38] After plasma reduction treatment, some of the surface Cu is reduced to metallic Cu,[39] showing the coexistence of zero-valent, monovalent, and divalent Cu species (Fig. 2a). For Cu_2O and Cu_2O–Ar/H_2, CuO originates from the inevitable oxidation of Cu species when exposed to air. Nevertheless, for Cu_2O–Ar/O_2, the presence of divalent copper on the surface results from the plasma oxidation treatment (Fig. 2a). Regarding the O 1s XPS spectrum, every O 1s curve is asymmetric and can be fitted into three components: lattice oxygen from Cu_2O ($O_L(Cu^+)$) at 530.3 eV or CuO ($O_L(Cu^{2+})$) at 529.5 eV,[40] adsorbed oxygen (O_{ad}) at 531.5 eV, and adsorbed water (H_2O_{ad}) at 533.5 eV[41,42] (Fig. 2b). The ratio between O_{ad} and O_L can be used to evaluate the amount of surface oxygen vacancies.[43] It can be observed that the oxygen vacancy content follows this order: Cu_2O–Ar/H_2 (3.95) > Cu_2O (2.54) > Cu_2O–Ar/O_2 (0.97), indicating that Cu_2O–Ar/H_2 has a higher density of surface oxygen vacancies compared to its other two counterparts.

Synchrotron-based X-ray absorption Near-Edge Structure (XANES) spectra and Extended X-ray Absorption Fine Structure (EXAFS) spectra were recorded to further study the chemical state and local coordination environment of copper sites. Compared to Cu_2O and CuO references, the XANES spectra of the as-synthesized samples display characteristics of Cu_2O (Fig. 2c). Although plasma reduction or oxidation treatments could affect the oxidation state of surface Cu atoms, the bulk phase of the catalysts retains attributes of Cu_2O. On the other hand, fitting in the *R*-space of EXAFS spectra of the as-prepared samples was then conducted to quantify changes in scattering paths (Fig. 2d and Table S1†). For the original Cu_2O sample, a Cu–O coordination number of 1.90 at 1.84 Å and Cu–Cu coordination number of 13.1 at 3.01 Å can be observed, similar to the Cu_2O reference, indicating the characteristic properties of Cu_2O. After plasma reduction or oxidation treatment, different Cu–O coordination numbers of 1.77 at 1.79 Å for Cu_2O–Ar/H_2 and 1.65 at 1.84 Å for Cu_2O–Ar/O_2 can be obtained, indicating that plasma treatment results in structural changes around Cu. For Cu_2O–Ar/H_2, the reduced Cu–O coordination number and similar Cu–Cu coordination number compared to the Cu_2O reference indicate the presence of oxygen vacancies. A wavelet transform was employed to elucidate the coordination environment near the Cu atoms and confirm the atomic distribution of Cu in all samples. As shown in Fig. 2e, for the Cu_2O reference, a strong wavelet transform signal focused at around 5 $Å^{-1}$ originating from Cu–O coordination is observed, while another intense signal at the same focus can be attributed to Cu–Cu coordination. The wavelet transform contour plot of the CuO reference exhibits only Cu–O coordination features (Fig. S9a†). In contrast, the original Cu_2O sample exhibits similar peak intensities and positions to the Cu_2O reference (Fig. S9b†), indicating their resemblance in structures.

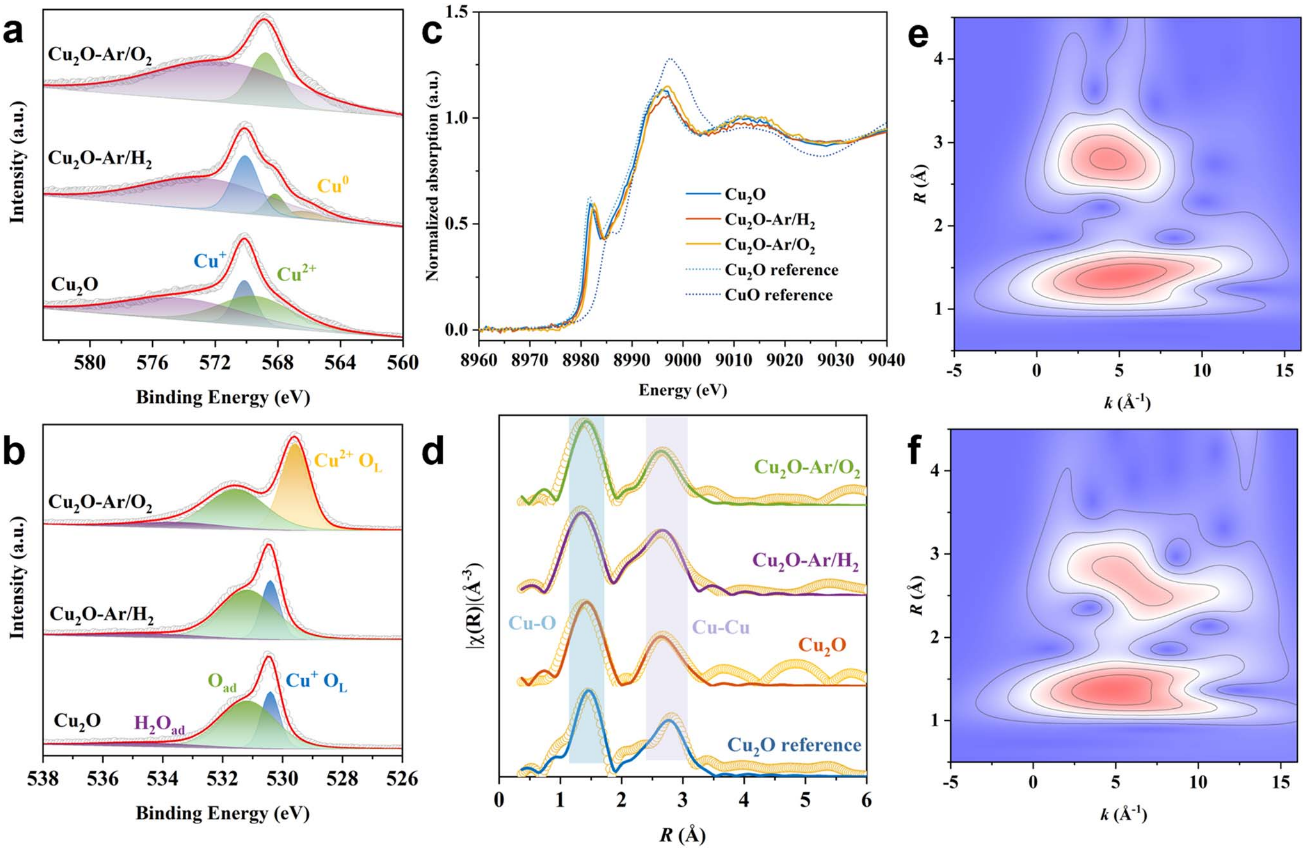

Fig. 2 *Ex situ* X-ray spectroscopic analysis of electrocatalysts. (a and b) Cu LMM Auger spectra (a) and O 1s XPS spectra (b) of the as-prepared catalysts; (c) Cu K-edge XANES spectra of Cu_2O, Cu_2O–Ar/H_2 and Cu_2O–Ar/O_2 samples and corresponding references (Cu_2O, and CuO). (d) Cu K-edge EXAFS experimental and fitting spectra of Cu_2O, Cu_2O–Ar/H_2 and Cu_2O–Ar/O_2 catalysts and corresponding references (Cu_2O). (e and f) Wavelet transforms for the k^3-weighted EXAFS signals of Cu_2O reference (e) and Cu_2O–Ar/H_2 (f).

However, after plasma reduction or oxidation treatment, differing first shell Cu–O and second shell Cu–Cu scattering distributions suggest variations in the local coordination environment around Cu between Cu_2O–Ar/H_2 and Cu_2O–Ar/O_2 (Fig. 2f *vs.* Fig. S9c†).

3.2 Electrochemical CO_2 reduction performance

The ECR performance of the as-synthesized catalysts was evaluated in a flow cell using an alkaline electrolyte (1 M KOH). All catalysts exhibit a similar reduced product distribution, with CO, methane, and formic acid as the main C_1 products and ethylene, ethanol, acetic acid, and isopropanol as the main C_{2+} products (Fig. 3a, S10a and b†). For all samples, the H_2 FE increases with increasing cathodic potentials, suggesting that at higher negative potentials, the competitive hydrogen evolution reaction (HER) suppresses the production of C_{2+} products. Therefore, all samples demonstrate higher C_{2+} product selectivity at lower potentials (-0.65 or -0.7 V_{RHE}). The Cu_2O sample shows a relatively high C_{2+} FE (70.47%) at -0.65 V_{RHE}, but as the potentials increase, the C_{2+} FE continues to decrease to 39% at -0.75 V_{RHE} (Fig. 3b). Increasing the cathode potentials induces the further reduction of Cu_2O to metallic Cu. Since oxidative Cu species act as the main active sites for C_{2+} products, the reduction in these active species on the catalyst surface results in a decrease in the selectivity for C_{2+} products. This indicates that *in situ* reduction of Cu_2O cannot enhance catalytic activity at higher cathodic potentials, possibly due to the inherent Cu_2O grain boundary structure's inability to stabilize active Cu^+ species. Although plasma oxidation treatment (Ar/O_2) raises the oxidation state of Cu_2O, achieving a C_{2+} FE of 77.14% at low potential (-0.65 V_{RHE}), it still fails to stabilize active Cu^+ species at higher potentials (-0.7 and -0.75 V_{RHE}), leading to decreased activity (Fig. 3b). However, for the Cu_2O–Ar/H_2 sample, the C_{2+} FE is lower than that of Cu_2O and Cu_2O–Ar/O_2 at -0.65 V_{RHE}, but at -0.7 V_{RHE}, the C_{2+} FE reaches 81.2% with a current density of ~100 mA cm^{-2}. Moreover, at higher potentials (-0.75 V_{RHE}), the C_{2+} FE of Cu_2O–Ar/H_2 also exceeds that of Cu_2O and Cu_2O–Ar/O_2 (Fig. 3b). This suggests that the Cu^0/Cu^+ interface structure and high density of oxygen vacancies obtained through plasma reduction treatment (Ar/H_2) can effectively stabilize active Cu species during ECR, enhancing C_{2+} selectivity. Considering the impact of plasma treatment on catalytic activity of C_{2+} products, a comparison is made with other plasma-treated catalysts in terms of C_{2+} FE (Fig. 3c and Table S2†). The results show that catalytic activity

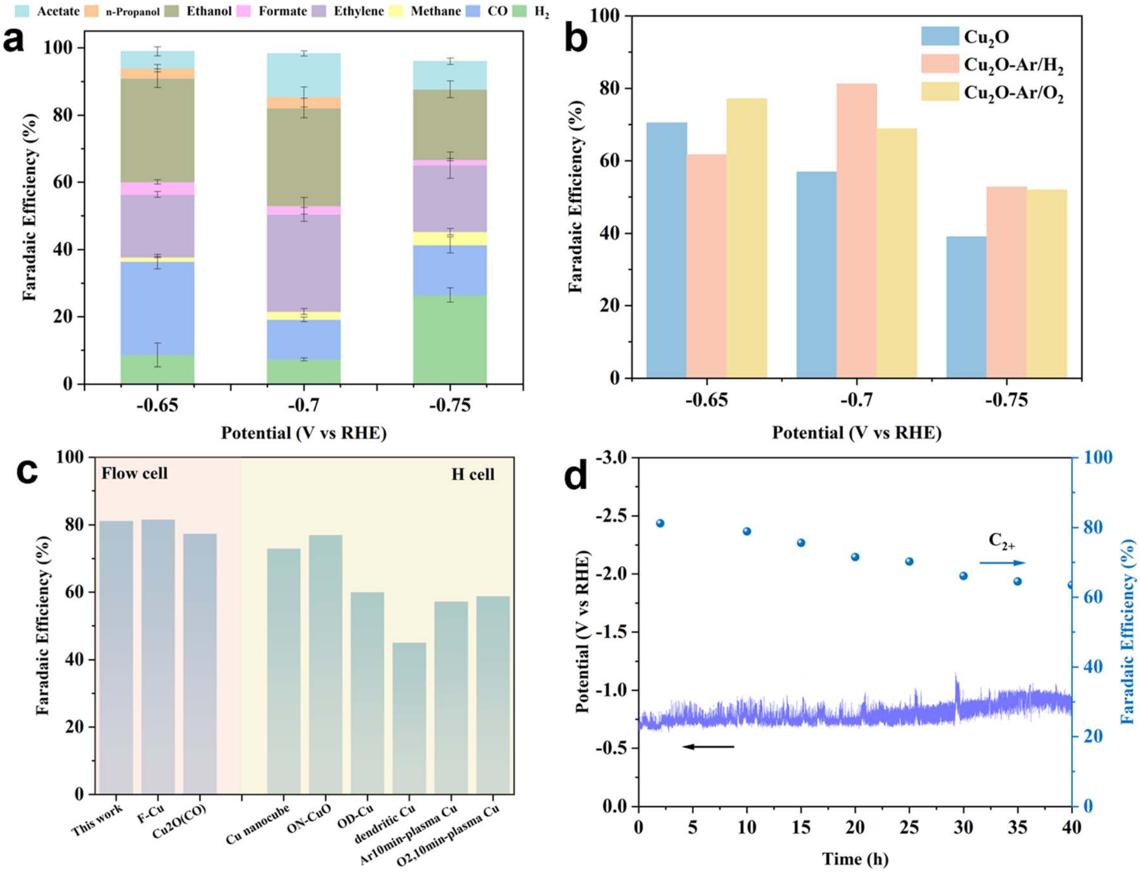

Fig. 3 ECR performance of the as-prepared catalysts. (a) The reduced product distribution of CO_2 for Cu_2O–Ar/H_2 at different cathodic potentials under ECR. (b) The FEs for C_{2+} products on the as-synthesized samples. (c) Comparisons of the FE values for C_{2+} products between Cu_2O–Ar/H_2 and other recently reported plasma-treated Cu-based catalysts. The summary of the specific ECR performance of catalysts is presented in Table S1.† (d) The stability test of Cu_2O–Ar/H_2 at a current density of 100 mA cm^{-2} using a flow cell.

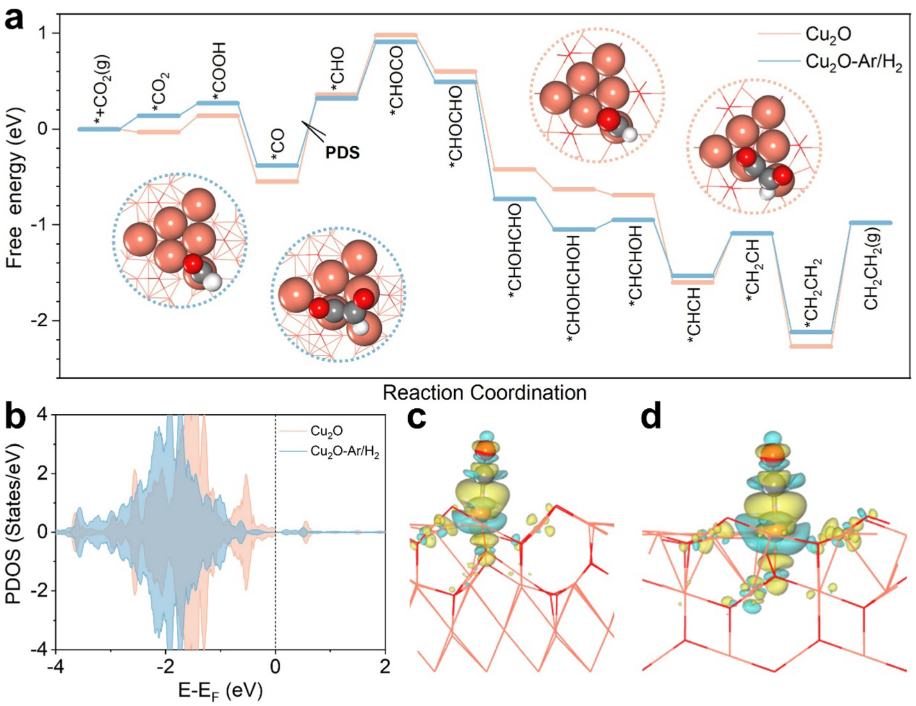

Fig. 4 DFT investigations. (a) Free energy profile of ethylene production on Cu$_2$O–Ar/H$_2$ and Cu$_2$O, including the *CHO and *CHOCO structures. (b) PDOS of the Cu-d states of vertex Cu atoms in Cu$_2$O–Ar/H$_2$ and Cu$_2$O. Charge density differences of *CO on (c) Cu$_2$O–Ar/H$_2$ and (d) Cu$_2$O with an isovalue of 0.001 e A^{-3}, where yellow and cyan regions denote electron accumulation and depletion, respectively.

of Cu$_2$O–Ar/H$_2$ exceeds that of most plasma-treated samples, demonstrating excellent ECR performance in terms of the C$_{2+}$ product pathway.

A long-term stability test was conducted to evaluate the practical applicability of the catalyst. Considering the C$_{2+}$ product selectivity and industrial-relevant current densities, Cu$_2$O–Ar/H$_2$ was selected to run stability tests in a flow cell with 1 M KOH at a constant current of 100 mA cm^{-2} (Fig. 3d). The results show that the ECR system could operate stably for 40 h, with a gradual decrease in C$_{2+}$ FE from an initial 81.2% to 63.5%. This indicates that Cu$_2$O–Ar/H$_2$ has significant potential for industrial-scale ECR to C$_{2+}$ product conversion as it can be used as a standardized process.

3.3 DFT calculations

To better understand how interface structures and oxygen vacancies enhance the activity towards C$_{2+}$ products, we conducted DFT calculations with ethylene as the representative C$_{2+}$ product. As shown in Fig. S11,† there are Cu triangles due to oxygen vacancies, of which both vertex and edge Cu atoms can be active sites. The project density of states (PDOS) shows that the Cu-d states of vertex atoms are always closer to the Fermi level than those of edge atoms (Fig. S12†), so CO$_2$ adsorption begins on these sites. For ethylene production, the adsorbed *CO$_2$ is reduced to *CO first and then hydrogenated to *CHO on vertex Cu atoms, and subsequently the C–C coupling occurs, *CHO + *CO → *CHOCO, on both vertex and edge Cu atoms (Fig. 4a). The C–C coupling step is always endothermic but is weaker than the hydrogenation of *CO to *CHO, and the potential-determining step (PDS) is thus *CO → *CHO, with the free energy changes of the PDS of 0.70 and 0.91 eV for Cu$_2$O–Ar/H$_2$ and Cu$_2$O, respectively. Fig. 4b shows the PDOS of vertex Cu atoms in Cu$_2$O–Ar/H$_2$ and Cu$_2$O, and we can find that the Cu-d states of Cu$_2$O–Ar/H$_2$ are more far to the Fermi level than those of Cu$_2$O, which leads to different adsorption strengths of *CO. Electron accumulation between active Cu sites and the C atom of *CO can be found in the charge density difference plots (Fig. 4c and d), validating strong interactions between *CO and catalysts. The Bader charge analysis suggests that 0.10 |e| is transferred from Cu$_2$O–Ar/H$_2$ to *CO, which is smaller than that on Cu$_2$O (0.16 |e|), in accordance with the more unactive Cu-d states of Cu$_2$O–Ar/H$_2$ shown in Fig. 4b. This leads to weaker *CO adsorption on Cu$_2$O–Ar/H$_2$ with $E_{\text{ads-CO}} = -1.58$ eV, while $E_{\text{ads-CO}} = -1.83$ eV for Cu$_2$O. In short, multiple active sites induced by oxygen vacancies make the C–C coupling easier than the *CO hydrogenation and weaker *CO adsorption on Cu$_2$O–Ar/H$_2$ related to interface engineering makes the *CO hydrogenation easier than that on Cu$_2$O.

4 Conclusions

In summary, a facile, scalable, and standardized magnetron sputtering method combined with plasma surface treatment was developed to controllably construct high-activity catalysts for C$_{2+}$ products. Cu$_2$O with rich grain boundaries, upon plasma reduction treatment, displays a well-defined Cu^0/Cu$^+$ interface structure with abundant oxygen vacancies. The enhanced activity stems from the synergistic interaction of the interface structure and oxygen vacancies. Compared to the original Cu_2O and Cu_2O further treated with plasma oxidation, pre-plasma reduction treatment of Cu_2O effectively prevents the loss of active sites during *in situ* reduction of ECR. This work reveals the real active sites created by plasma treatment during the ECR process, effectively promoting the industrial-scale application of ECR.

Data availability

The authors declare that all data supporting this study are available within the paper and ESI† files. Source data are provided upon request.

Author contributions

Y. A. W. conceived and supervised the project. Z. T. co-supervised the project. C. V. S. and L. Z. led the DFT calculations. S. J. and Y. Z. carried out the catalyst's synthesis. L. W. conducted characterization and performance tests of catalysts. X. Y. and C. Q. conducted the DFT calculations. S. J. carried out the XAS measurements. N. C. provided advice for the XAFS measurements. L. W., X. Y., S. J., C. V. S., Z. C. T., and Y. A. W. wrote the manuscript. All authors made comments and revised the manuscript.

Conflicts of interest

All the authors declare no competing interests.

Acknowledgements

Y. A. W. acknowledges the funding from the Government of Canada's New Frontiers Research Fund-Transformation CANSTOREnergy Project (NFRFT-2022-00197), the Natural Sciences and Engineering Research Council of Canada (NSERC) (RGPIN-2020-05903 and GECR-2020-00476), the Tang Family Chair in New Energy Materials and Sustainability, the Canadian Foundation for Innovation John R. Evans Leaders Fund (#41779), and the Ontario Research Fund for Small Infrastructure (#41779). Z. T. acknowledges the funding from the NSERC collaborative research and treating experience program (CREATE) and GCI Ventures Capital, Toronto. This research used the resources of the Canadian Light Source and its funding partners. The studies for hard XAS were performed at HXMA beamlines of the Canadian Light Source (CLS), a national research facility of the University of Saskatchewan, which is supported by the Canada Foundation for Innovation (CFI), the Natural Sciences and Engineering Research Council (NSERC), the National Research Council (NRC), the Canadian Institutes of Health Research (CIHR), and the Government of Saskatchewan. C. V. S. acknowledges support of the Natural Sciences & Engineering Research Council of Canada (NSERC), University of Toronto, and the Digital Research Alliance of Canada for enabling DFT simulations.

References

1 C. P. O'Brien, *et al.*, CO_2 Electrolyzers, *Chem. Rev.*, 2024, **124**, 3648–3693.
2 L. Peng, *et al.*, Research advances in electrocatalysts, electrolytes, reactors and membranes for the electrocatalytic carbon dioxide reduction reaction, *Acta Phys.–Chim. Sin.*, 2023, **39**(12), 2302037.
3 Y. Jia, *et al.*, Cu-based bimetallic electrocatalysts for CO_2 reduction, *Adv. Powder Mater.*, 2022, **1**(1), 100012.
4 L. Fan, *et al.*, Strategies in catalysts and electrolyzer design for electrochemical CO_2 reduction toward C_{2+} products, *Sci. Adv.*, 2020, **6**(8), eaay3111.
5 L. Fan, *et al.*, 1D SnO_2 with Wire-in-Tube Architectures for Highly Selective Electrochemical Reduction of CO_2 to C_1 Products, *Adv. Funct. Mater.*, 2018, **28**(17), 1706289.
6 S. Verma, *et al.*, The effect of electrolyte composition on the electroreduction of CO_2 to CO on Ag based gas diffusion electrodes, *Phys. Chem. Chem. Phys.*, 2016, **18**(10), 7075–7084.
7 W. Ma, *et al.*, Electrocatalytic reduction of CO_2 and CO to multi-carbon compounds over Cu-based catalysts, *Chem. Soc. Rev.*, 2021, **50**(23), 12897–12914.
8 M. Ma, *et al.*, Controllable hydrocarbon formation from the electrochemical reduction of CO_2 over Cu nanowire arrays, *Angew. Chem. Int. Ed.*, 2016, **55**(23), 6680–6684.
9 C. W. Li, *et al.*, Electroreduction of carbon monoxide to liquid fuel on oxide-derived nanocrystalline copper, *Nature*, 2014, **508**(7497), 504–507.
10 X. Chang, *et al.*, Tuning Cu/Cu_2O interfaces for the reduction of carbon dioxide to methanol in aqueous solutions, *Angew. Chem.*, 2018, **130**(47), 15641–15645.
11 X. Y. Zhang, *et al.*, Direct OC–CHO coupling towards highly C_{2+} products selective electroreduction over stable Cu^0/Cu^{2+} interface, *Nat. Commun.*, 2023, **14**(1), 7681.
12 W. J. Dong, *et al.*, Grain Boundary Engineering of Cu–Ag Thin-Film Catalysts for Selective (Photo) Electrochemical CO_2 Reduction to CO and CH_4, *ACS Appl. Mater. Interfaces*, 2021, **13**(16), 18905–18913.
13 Z. Chang, *et al.*, The tunable and highly selective reduction products on Ag@Cu bimetallic catalysts toward CO_2 electrochemical reduction reaction, *J. Phys. Chem. C*, 2017, **121**(21), 11368–11379.
14 J. Chen and L. Wang, Effects of the catalyst dynamic changes and influence of the reaction environment on the performance of electrochemical CO_2 reduction, *Adv. Mater.*, 2022, **34**(25), 2103900.
15 Q. Wu, *et al.*, Nanograin-Boundary-Abundant Cu_2O–Cu Nanocubes with High C_{2+} Selectivity and Good Stability during Electrochemical CO_2 Reduction at a Current Density of 500 mA cm^{-2}, *ACS Nano*, 2023, **17**, 12884–12894.
16 Y. Yang, *et al.*, Operando studies reveal active Cu nanograins for CO_2 electroreduction, *Nature*, 2023, **614**(7947), 262–269.
17 X. Yuan, *et al.*, Controllable Cu^0–Cu^+ sites for electrocatalytic reduction of carbon dioxide, *Angew. Chem.*, 2021, **133**(28), 15472–15475.

18 H. Li, *et al.*, Oxygen vacancy structure associated photocatalytic water oxidation of BiOCl, *ACS Catal.*, 2016, **6**(12), 8276–8285.

19 H. Li, *et al.*, Oxygen vacancy-mediated photocatalysis of BiOCl: reactivity, selectivity, and perspectives, *Angew. Chem. Int. Ed.*, 2018, **57**(1), 122–138.

20 X. Li, *et al.*, Strategies for enhancing electrochemical CO_2 reduction to multi-carbon fuels on copper, *Innov. Mater.*, 2023, **1**(1), 100014.

21 Z. Gu, *et al.*, Oxygen vacancy tuning toward efficient electrocatalytic CO_2 reduction to C_2H_4, *Small Methods*, 2019, **3**(2), 1800449.

22 Y. Wang, *et al.*, Defect and interface engineering for aqueous electrocatalytic CO_2 reduction, *Joule*, 2018, **2**(12), 2551–2582.

23 J.-J. Zou, *et al.*, Control of the metal – support interface of NiO-loaded photocatalysts *via* cold plasma treatment, *Langmuir*, 2006, **22**(5), 2334–2339.

24 D. G. Park, *et al.*, Increasing CO binding energy and defects by preserving Cu oxidation state *via* O_2-plasma-assisted N doping on CuO enables high C_{2+} selectivity and long-term stability in electrochemical CO_2 reduction, *ACS Catal.*, 2023, **13**(13), 9222–9233.

25 Y. Zhou, *et al.*, Dopant-induced electronic structure modification of HOPG surfaces: implications for high activity fuel cell catalysts, *J. Phys. Chem. C*, 2010, **114**(1), 506–515.

26 H. Mistry, *et al.*, Highly selective plasma-activated copper catalysts for carbon dioxide reduction to ethylene, *Nat. Commun.*, 2016, **7**(1), 1–9.

27 D. Gao, *et al.*, Plasma-activated copper nanocube catalysts for efficient carbon dioxide electroreduction to hydrocarbons and alcohols, *ACS Nano*, 2017, **11**(5), 4825–4831.

28 P. Chen, *et al.*, *In situ* reconfiguration of plasma-engineered copper electrodes towards efficient electrocatalytic hydrogenation, *Catal. Sci. Technol.*, 2022, **12**(12), 4032–4039.

29 F. Scholten, *et al.*, Plasma-modified dendritic Cu catalyst for CO_2 electroreduction, *ACS Catal.*, 2019, **9**(6), 5496–5502.

30 J. P. Perdew, *et al.*, Generalized Gradient Approximation Made Simple, *Phys. Rev. Lett.*, 1996, **77**(18), 3865–3868.

31 G. Kresse and J. Furthmüller, Efficiency of *ab initio* total energy calculations for metals and semiconductors using a plane-wave basis set, *Comput. Mater. Sci.*, 1996, **6**(1), 15–50.

32 S. Grimme, *et al.*, A consistent and accurate *ab initio* parametrization of density functional dispersion correction (DFT-D) for the 94 elements H-Pu, *J. Chem. Phys.*, 2010, **132**(15), 154104.

33 K. Mathew, *et al.*, Implicit solvation model for density-functional study of nanocrystal surfaces and reaction pathways, *J. Chem. Phys.*, 2014, **140**, 084106.

34 C. Chen, *et al.*, The *in situ* study of surface species and structures of oxide-derived copper catalysts for electrochemical CO_2 reduction, *Chem. Sci.*, 2021, **12**(16), 5938–5943.

35 Z. Zhou, *et al.*, Enhanced CO_2 Electroreduction to Multi-Carbon Products on Copper *via* Plasma Fluorination, *Adv. Sci.*, 2024, 2309963.

36 C. Ma, *et al.*, A novel core/shell cuprous oxide-based structure with improved microwave absorbing and antibacterial performance, *J. Clean. Prod.*, 2022, **378**, 134419.

37 Y.-H. Zhang, *et al.*, Oxygen vacancies in concave cubes Cu_2 O-reduced graphene oxide heterojunction with enhanced photocatalytic H_2 production, *J. Mater. Sci.: Mater. Electron.*, 2019, **30**, 7182–7193.

38 I. Platzman, *et al.*, Oxidation of polycrystalline copper thin films at ambient conditions, *J. Phys. Chem. C*, 2008, **112**(4), 1101–1108.

39 Y. Yang, *et al.*, Nitrogen-doping boosts *CO utilization and H_2O activation on copper for improving CO_2 reduction to C_{2+} products, *Green Energy Environ.*, 2023, in press.

40 Y. Wang, *et al.*, Synthesis of porous Cu_2 O/CuO cages using Cu-based metal–organic frameworks as templates and their gas-sensing properties, *J. Mater. Chem. A*, 2015, **3**(24), 12796–12803.

41 L. Xue, *et al.*, Unveiling the reaction pathway on Cu/CeO_2 catalyst for electrocatalytic CO_2 reduction to CH_4, *Appl. Catal., B*, 2022, **304**, 120951.

42 Q. T. Trinh, *et al.*, Synergistic application of XPS and DFT to investigate metal oxide surface catalysis, *J. Phys. Chem. C*, 2018, **122**(39), 22397–22406.

43 Z. Wang, *et al.*, Surface oxygen vacancies on Co_3 O_4 mediated catalytic formaldehyde oxidation at room temperature, *Catal. Sci. Technol.*, 2016, **6**(11), 3845–3853.